

Coherence-enhanced thermodynamic performance in a periodically-driven inelastic heat engine

Jincheng Lu,¹ Zi Wang,² Jie Ren,² Chen Wang,^{3,*} and Jian-Hua Jiang^{4,†}

¹*Jiangsu Key Laboratory of Micro and Nano Heat Fluid Flow Technology and Energy Application, School of Physical Science and Technology, Suzhou University of Science and Technology, Suzhou, 215009, China*

²*Center for Phononics and Thermal Energy Science, China-EU Joint Center for Nanophononics, Shanghai Key Laboratory of Special Artificial Microstructure Materials and Technology, School of Physics Science and Engineering, Tongji University, Shanghai 200092 China*

³*Department of Physics, Zhejiang Normal University, Jinhua, Zhejiang 321004, China*

⁴*Suzhou Institute of Advanced Research, University of Science and Technology of China, Suzhou, 215123, China*

(Dated: February 27, 2024)

Quantum thermodynamics with microscopic inelastic scattering processes has been intensively investigated in recent years. Here, we apply quantum master equation combined with full counting statistics approach to investigate the role of quantum coherence on the periodically-driven inelastic heat engine. We demonstrate that the inelastic quantum heat engine exhibits dramatic advantage of thermodynamic performance compared to their elastic counterpart. Moreover, it is found that inelastic currents, output work, and the efficiency can be enhanced by quantum coherence. In particular, the geometric effect proves crucial in achieving maximal values of generated output work and energy conversion efficiency. The Berry curvature boosted by quantum coherence unveils the underlying mechanism of periodically-driven inelastic heat engine. Our findings may provide some insights for further understanding and optimizing periodically-driven heat engines via quantum coherence resource and inelastic scattering processes.

I. INTRODUCTION

Quantum thermodynamics, an exquisite combination of thermodynamics and quantum mechanics, addresses heat-to-work conversion and entropy production in quantum thermal machines at the microscopic level, ranging from the heat engines, refrigerators, heat pumps, and even multitask machines [1–4]. The practical quantum thermodynamics mainly considers nonequilibrium thermodynamic processes, which are typically realized by (i) time-dependent modulations [5, 6]; (ii) multiple reservoirs with thermodynamic bias [7–9]; (iii) quantum measurements [10, 11]; (iv) quantum information, e.g., quantum correlation [12–14]. The periodically driven quantum heat engines have attracted increasing attention, which can overcome thermodynamic biases to sustain the heat transfer from the cold (low voltage) drain to the hot (high voltage) source, thereby enabling the thermodynamic operations [15–22]. In particular, the geometric effects [23, 24], e.g., Berry phase and quantum metric, should be properly adopted.

Quantum coherence is one kind of indispensable ingredients for quantum mechanics and also a fundamental

quantum resource in quantum thermodynamics, which distinguish from classical counterparts [25, 26]. With its unique features, quantum coherence finds fertile applications in quantum thermal machines [27–36]. Notably, heat engine, heat pump, and multitask thermal machine can be driven by pure quantum coherence [37–39]. Quantum coherence can also enhance the efficiency and constancy of the quantum thermal machines [40]. Moreover, quantum coherence enables us to explore the quantum contribution to the nonequilibrium entropy production and information processes, e.g., nonequilibrium Landauer principle [41, 42].

Recently, there has been a growing recognition of the significance of inelastic scattering processes in nonequilibrium transport and thermodynamics [43–47], which are implemented in three-terminal setups, in contrast to the elastic scattering processes sufficiently realized via two terminals. The generic inelastic processes enable one to investigate nonlinearly-coupled electronic and bosonic currents. Interestingly, it is found that the bounds of Onsager coefficient with inelastic processes are dramatically relaxed to promote the thermodynamic performance [48]. Thus, quantum thermal machines (e.g., thermal transistor and refrigerator) exhibit thermodynamic advantage by comparing with counterparts under elastic processes. Meanwhile, such microscopic inelastic processes yield other unconventional transport and thermodynamic

* wangchen@zjnu.cn

† joejhjiang@hotmail.com

phenomena, e.g., cooling by heating [49], the separation of charge and heat currents [50, 51], linear transistor effects [52, 53], and cooperative heat engines [54]. Though extensive studies have been conducted to excavate the steady-state thermodynamics of inelastic quantum thermal machines [55], the influence of interplay between quantum coherence and geometric effects on thermodynamic performance of periodically-driven quantum heat engines are far from clear.

In our work, we have conducted a comprehensive study to investigate the impact of quantum coherence on thermodynamic performance of a periodically driven heat engine modulated in adiabatic regimes, by including the Redfield equation in absence of secular approximation. First, the performance of a three-terminal inelastic quantum heat engine is compared with a two-terminal elastic counterpart to demonstrate the advantages of inelastic scattering processes. Then, the geometric and dynamic current components dramatically affected by quantum coherence are obtained, and the contribution of the geometric component to the thermodynamic performance of three-terminal heat engine is rigorously analyzed.

The main points of this work are demonstrated as: (i) The Redfield equation encompasses a unified description of nonlinear electronic and phononic transport in a three-terminal periodically-driven setup, with a particular focus on the interplay between inelastic electron-phonon scattering and quantum coherence on nonequilibrium currents. Thus the method goes beyond the traditional transport approaches, e.g., Fermi-golden rule [43, 56], the Lindblad equation [57, 58], and Redfield equation with secular approximation [59]. (ii) The three-terminal driven inelastic quantum heat engine exhibits significant advantage of thermodynamic performance in a wide parameter regime, compared to two-terminal elastic counterpart [60, 61]. This clearly demonstrates the importance role of the inelastic scattering processes on driven quantum thermodynamics. Additionally, the combination of heat and particle transports in inelastic transport facilitates concurrent optimization of thermal conductance and electrical conductance for thermodynamic devices. (iii) The thermodynamic performance of the driven inelastic heat engine can be dramatically enhanced via quantum coherence. The nonequilibrium currents are decomposed as dynamic and geometric components. And the geometric component is found to be crucial in achieving maximal values of generated output work and thermodynamic efficiency.

This study is structured as follows: In Sec. II, we describe the setup of the inelastic heat engines and derive the dynamic, geometric currents using the quantum mas-

ter equation with a full counting statistics approach. The work and efficiency also have been defined. In Sec. III, we focus on analyzing the energy efficiency and output work of the inelastic heat engines. Additionally, we numerically compare the results with both the elastic engine and the incoherent engine. We summarize our findings in Sec. IV. For simplicity, we set $\hbar = k_B = e \equiv 1$ throughout this paper.

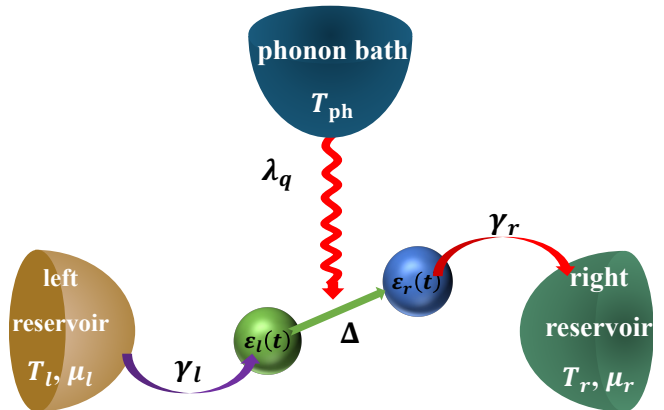


FIG. 1. Illustration of the three-terminal inelastic heat engine: An electron initially departs from the left reservoir and enters the left QD, characterized by an energy level ε_l . Subsequently, the electron undergoes a transition to the right QD, which possesses a different energy level denoted as ε_r . This transition is facilitated by interacting with one phonon from the phonon bath, maintained at a temperature of T_{ph} . Within this setup, two electric reservoirs are involved, each characterized by distinct temperatures and chemical potentials. The left (l) and right (r) electric reservoirs have temperatures denoted as $T_{l(r)}$, while their respective chemical potentials are represented as $\mu_{l(r)}$. Δ represents the tunneling strength between two QDs, γ_i characterizes the coupling between the electronic reservoirs and the corresponding QD, and λ_q represents the electron-phonon interaction strength.

II. MODEL AND METHODS

A. Inelastic heat engine

We consider an inelastic heat engine, which is composed of a double quantum dot (QD) system inelastically coupled to a phonon bath, and each dot individually exchanges energy with an electronic reservoir

(e.g., metal lead, denoted as l and r), as shown in Fig. 1. The Hamiltonian of this inelastic heat engine reads $\hat{H} = \hat{H}_{\text{DQD}} + \hat{H}_{\text{e-ph}} + \hat{H}_{\text{lead}} + \hat{H}_{\text{tun}} + \hat{H}_{\text{ph}}$ [46]. Specifically, the double QDs is described as

$$\hat{H}_{\text{DQD}} = \sum_{i=l,r} \varepsilon_i \hat{d}_i^\dagger \hat{d}_i + \Delta(\hat{d}_l^\dagger \hat{d}_r + \text{H.c.}), \quad (1)$$

where \hat{d}_i^\dagger (\hat{d}_i) is the creation (annihilation) operator of one electron in the i -th QD, ε_i represents the QD energy, and Δ shows tunneling between the two QDs. The phonon reservoir denotes $\hat{H}_{\text{ph}} = \sum_q \omega_q \hat{a}_q^\dagger \hat{a}_q$, where \hat{a}_q^\dagger (\hat{a}_q) creates (annihilates) one phonon with the frequency ω_q . The inelastic electron-phonon interaction is described as

$$\hat{H}_{\text{e-ph}} = \sum_q \lambda_q \hat{d}_l^\dagger \hat{d}_r (\hat{a}_q + \hat{a}_q^\dagger) + \text{H.c.}, \quad (2)$$

where λ_q is the strength of the electron-phonon coupling strength. The electronic leads are expressed as $\hat{H}_{\text{lead}} = \sum_{j=L,R} \sum_k \varepsilon_{jk} N_{jk}$, with the electron number $N_{jk} = \hat{d}_{jk}^\dagger \hat{d}_{jk}$ in the j -th lead at the momentum k . The electron tunneling between the dots and the electronic reservoirs are given by $\hat{H}_{\text{tun}} = \sum_{j=L,R;k} \gamma_{jk} \hat{d}_j^\dagger \hat{d}_{jk} + \text{H.c.}$, where γ_{jk} is the corresponding coupling strength.

To analyze the heat engine in eigenspace of the double QDs, we begin to diagonalize \hat{H}_{DQD} as

$$\hat{H}_{\text{DQD}} = E_D \hat{D}^\dagger \hat{D} + E_d \hat{d}^\dagger \hat{d}, \quad (3)$$

where the eigenenergies denote $E_D = \frac{\varepsilon_r + \varepsilon_l}{2} + \sqrt{\frac{(\varepsilon_r - \varepsilon_l)^2}{4} + \Delta^2}$ and $E_d = \frac{\varepsilon_r + \varepsilon_l}{2} - \sqrt{\frac{(\varepsilon_r - \varepsilon_l)^2}{4} + \Delta^2}$, and the new sets of Fermion operators are specified as $\hat{D} = \sin \theta \hat{d}_l + \cos \theta \hat{d}_r$ and $\hat{d} = \cos \theta \hat{d}_l - \sin \theta \hat{d}_r$ [53, 61], with $\theta \equiv \arctan\left(\frac{2\Delta}{\varepsilon_r - \varepsilon_l}\right)/2$. Consequently, the electron-phonon and dot-reservoir tunneling terms are reexpressed as $\hat{H}_{\text{e-ph}} = \sum_q \lambda_q [\sin(2\theta)(\hat{D}^\dagger \hat{D} - \hat{d}^\dagger \hat{d}) + \cos(2\theta)(\hat{d}^\dagger D + D^\dagger \hat{d})](\hat{a}_q^\dagger + \hat{a}_q)$ and $\hat{H}_{\text{tun}} = \sum_k [\gamma_{Lk}(\sin \theta \hat{D}^\dagger + \cos \theta \hat{d}^\dagger) \hat{d}_{Lk} + \gamma_{Rk}(\cos \theta \hat{D}^\dagger - \sin \theta \hat{d}^\dagger) \hat{d}_{Rk}] + \text{H.c.}$. From the term $\hat{H}_{\text{e-ph}}$ it is known that in the eigenbasis of \hat{H}_{DQD} there both exist dephasing and damping processes, which may generate the steady-state coherence [62].

B. Geometric-phase-induced currents

Full counting statistics nowadays is widely accepted as a powerful utility to characterize complete information of current fluctuations [63]. Based on two-time measurement protocol [64], we apply the full counting statistics to obtain the particle and energy flows out of electronic

reservoirs and heat current out of phonon reservoir by including $\mathbf{\Lambda} = \{\lambda_p, \lambda_E, \lambda_{\text{ph}}\}$, respectively (see the introduction of full counting statistics in Appendix A). Consequently, the counting-field-dependent total Hamiltonian is described as

$$H_{-\mathbf{\Lambda}/2} = H_{\text{DQD}} + H_{\text{ph}} + H_{\text{lead}} + V_{-\mathbf{\Lambda}/2}, \quad (4)$$

with $V_{-\mathbf{\Lambda}/2}$ specified as

$$\begin{aligned} V_{-\mathbf{\Lambda}/2} = & \sum_q \lambda_q [\sin(2\theta)(\hat{D}^\dagger \hat{D} - \hat{d}^\dagger \hat{d}) \\ & + \cos(2\theta)(\hat{d}^\dagger D + D^\dagger \hat{d})] (e^{i\frac{\lambda_{\text{ph}}}{2}\omega_q} \hat{a}_q + \text{H.c.}) \\ & + \sum_k ([\gamma_{Lk}(\sin \theta \hat{D}^\dagger + \cos \theta \hat{d}^\dagger) \hat{d}_{Lk} \\ & + \gamma_{Rk} e^{-i\frac{\lambda_p}{2} - i\frac{\lambda_E}{2} \varepsilon_{Rk}} (\cos \theta \hat{D}^\dagger - \sin \theta \hat{d}^\dagger) \hat{d}_{Rk}] + \text{H.c.}). \end{aligned} \quad (5)$$

We assume the electron-phonon coupling and dot-reservoir tunnelings are weak. Based on the Born-Markov approximation, we perturb $V_{-\mathbf{\Lambda}/2}$ to obtain the quantum master equation as [65]

$$\begin{aligned} \frac{\partial}{\partial t} \rho_S(\mathbf{\Lambda}, t) = & i[\rho_S(\mathbf{\Lambda}, t), H_{\text{DQD}}] \\ & - \int_0^\infty d\tau \text{Tr}_B \{ [[V_{-\mathbf{\Lambda}/2}, [V_{-\mathbf{\Lambda}/2}(-\tau), \rho_S(\mathbf{\Lambda}, t) \otimes \rho_B]_{\mathbf{\Lambda}}]_{\mathbf{\Lambda}} \}, \end{aligned} \quad (6)$$

where $\rho_S(\mathbf{\Lambda}, t)$ denotes the reduced density operator of central double QDs system with counting parameters, i.e. $\rho_S(\mathbf{\Lambda}, t) = \text{Tr}_B \{ \rho_{\mathbf{\Lambda}}^T(t) \}$, with $\rho_{\mathbf{\Lambda}}^T(t)$ (see Eq. (A4) in Appendix A) the full density operator of the whole inelastic heat engine, the commuting relation denotes $[\hat{A}_{\mathbf{\Lambda}}, \hat{B}_{\mathbf{\Lambda}}]_{\mathbf{\Lambda}} = \hat{A}_{\mathbf{\Lambda}} \hat{B}_{\mathbf{\Lambda}} - \hat{B}_{\mathbf{\Lambda}} \hat{A}_{-\mathbf{\Lambda}}$, and the equilibrium distribution of reservoirs is specified as $\rho_B = \rho_l \otimes \rho_r \otimes \rho_{\text{ph}}$, with $\rho_i = \exp[-\beta_i(\hat{H}_i - \mu_i \hat{N}_i)] / Z_i$ ($i = l, r$), $\rho_{\text{ph}} = \exp[-\beta_{\text{ph}} \hat{H}_{\text{ph}}] / Z_{\text{ph}}$, the partition functions $Z_i = \text{Tr} \{ \exp[-\beta_i(\hat{H}_i - \mu_i \hat{N}_i)] \}$ and $Z_{\text{ph}} = \text{Tr} \{ \exp[-\beta_{\text{ph}} \hat{H}_{\text{ph}}] \}$, and the inverse temperatures $\beta_i = 1/k_B T_i$ and $\beta_{\text{ph}} = 1/k_B T_{\text{ph}}$. If we reorganize $\rho_S(\mathbf{\Lambda}, t)$ in the vector form $|\mathbf{P}(\mathbf{\Lambda}, t)\rangle = [|0\rangle \rho_S(\mathbf{\Lambda}, t) |0\rangle; \langle D | \rho_S(\mathbf{\Lambda}, t) | D \rangle; \langle d | \rho_S(\mathbf{\Lambda}, t) | d \rangle; \langle D | \rho_S(\mathbf{\Lambda}, t) | d \rangle; \langle d | \rho_S(\mathbf{\Lambda}, t) | D \rangle]$, the quantum master equation is reexpressed as

$$\frac{d|\mathbf{P}(\mathbf{\Lambda}, t)\rangle}{dt} = \mathbf{H}(\mathbf{\Lambda}, t) |\mathbf{P}(\mathbf{\Lambda}, t)\rangle, \quad (7)$$

where $\mathbf{H}(\mathbf{\Lambda}, t)$ is the evolution matrix with its elements shown in Appendix B. We note that the inclusion of the off-diagonal elements of the density matrix, i.e.,

$\langle D|\rho_S(\mathbf{\Lambda}, t)|d\rangle$ and $\langle d|\rho_S(\mathbf{\Lambda}, t)|D\rangle$, are the signature of quantum coherence. Conversely, if we neglect the quantum coherence effect, we disregard the off-diagonal elements.

For the heat engine modulated by parameters such as $\Gamma_i(t)$, $\mu_i(t)$, $T_i(t)$, and $\varepsilon_i(t)$ ($i = l, r$), in the long time evolution the cumulant generating function based on the large deviation principle and adiabatic perturbation theory can be divided into two components [66]

$$\mathcal{G}_{\text{tot}}(\mathbf{\Lambda}) = \mathcal{G}_{\text{dyn}}(\mathbf{\Lambda}) + \mathcal{G}_{\text{geo}}(\mathbf{\Lambda}), \quad (8)$$

where the dynamical phase denotes $\mathcal{G}_{\text{dyn}}(\mathbf{\Lambda}) = \frac{1}{\mathcal{T}} \int_0^{\mathcal{T}} dt E_g(\mathbf{\Lambda}, t)$, with $E_g(\mathbf{\Lambda}, t)$ the eigenvalue of $\mathbf{H}(\mathbf{\Lambda}, t)$ owning the maximum real part [66, 67], and the geometric phase is specified as $\mathcal{G}_{\text{geo}}(\mathbf{\Lambda}) = -\frac{1}{\mathcal{T}} \int_0^{\mathcal{T}} dt \langle \varphi(\mathbf{\Lambda}, t) | \partial_t | \psi(\mathbf{\Lambda}, t) \rangle$, with $\langle \varphi(\mathbf{\Lambda}, t) |$ and $| \psi(\mathbf{\Lambda}, t) \rangle$ left and right eigenvectors of $\mathbf{H}(\mathbf{\Lambda}, t)$. The dynamical component, \mathcal{G}_{dyn} , characterizes the temporal average and delineates the dynamic aspects of particle and heat transfer. While the geometric contribution, \mathcal{G}_{geo} , arises from adiabatic cyclic evolution and necessitates a minimum of two parameter modulations to manifest its effects [66–68].

Consequently, the particle current flowing from the right reservoir into the system is given by [55]:

$$\langle N_l \rangle = \left. \frac{\partial \mathcal{G}_{\text{tot}}(\mathbf{\Lambda})}{\partial(i\lambda_p)} \right|_{\mathbf{\Lambda}=0}, \quad (9)$$

and the particle flow from the left reservoir can be straightforwardly obtained as $\langle N_l \rangle = -\langle N_r \rangle$ via the law of particle conservation. Meanwhile the energy flow is expressed as

$$\langle E_r \rangle = \left. \frac{\partial \mathcal{G}_{\text{tot}}(\mathbf{\Lambda})}{\partial(i\lambda_E)} \right|_{\mathbf{\Lambda}=0}, \quad (10)$$

and electronic heat flow extracted from the right reservoir is defined as $\langle Q_r \rangle = \langle E_r \rangle - \mu_r \langle N_r \rangle$ [69]. The phononic heat current is given by

$$\langle Q_{\text{ph}} \rangle = \left. \frac{\partial \mathcal{G}_{\text{tot}}(\mathbf{\Lambda})}{\partial(i\lambda_{\text{ph}})} \right|_{\mathbf{\Lambda}=0}. \quad (11)$$

In analogy, the particle current $\langle N_l \rangle$ and energy current $\langle E_l \rangle$ flowing from the left electronic reservoir into the central system. In this study, we constrain all parameters of the driving protocol to an adiabatic driving regime: the driving period is chosen as $\mathcal{T} = 10^{-12}$ s, corresponding to $\hbar\Omega \approx 4 \times 10^{-2}$ meV. It's evident that the rate between system and reservoir $\Gamma_i = 4$ meV ($i = l, r, \text{ph}$), which is much greater than $\hbar\Omega$, and the adiabatic approximation

remains valid [18]. In this work, we demonstrate the realization of the thermoelectric engine in the double quantum dot system by choosing the left and right quantum dot energies, i.e., ε_l and ε_r , as the modulating parameters [22, 60, 70]. The quantum dots are driven adiabatically following the protocol: $\varepsilon_l = E_{A,l} + E_{B,l} \sin(\Omega t)$, $\varepsilon_r = E_{A,r} + E_{B,r} \sin(\Omega t + \phi)$. The impact of geometric properties can be realized by tuning the phase ϕ . Nonzero modulation phase ϕ is required to pump heat from one reservoir to another reservoir. Distinct values of ϕ correspond to different driving protocols. When $\phi = \pi/2$, the modulation induced geometric pump is optimized. In contrast, when $\phi = 0$, the geometric contribution diminishes, leaving only the dynamical counterpart. This stems from the disappearance of the enclosed area in the parameter space, e.g., ε_l and ε_r .

C. Definitions of work and efficiency

We operate the three-terminal inelastic heat engine by harvesting energy from the hot phonon reservoir with a fixed temperature of $k_B T_l = k_B T_r = 10$ meV and $k_B T_{\text{ph}} = 12$ meV and converting it into useful output work. The electrochemical potential bias is defined as $\Delta\mu = \mu_l - \mu_r$, with the average chemical potential $\mu \equiv (\mu_l + \mu_r)/2$. The particle and energy conservation laws imply that [16, 18],

$$\langle W_I \rangle = -(\langle E_l \rangle + \langle E_r \rangle + \langle Q_{\text{ph}} \rangle). \quad (12)$$

Here, $\langle W_I \rangle$ represents the input work per modulating period \mathcal{T} , which becomes vanishing once the driving is removed. And the useful output work of the heat engine is described as

$$\langle W_{\text{out}} \rangle = (\mu_l - \mu_r) \langle N_r \rangle. \quad (13)$$

The entropy production of the whole system is given by $\langle S \rangle = -\sum_{v=l,r,\text{ph}} \langle Q_v \rangle / T_v$ [71]. Moreover, the entropy production takes on a specific form [71]

$$T_l \langle S \rangle = (1 - T_l/T_{\text{ph}}) \langle Q_{\text{ph}} \rangle - \langle W_{\text{out}} \rangle + \langle W_I \rangle. \quad (14)$$

From the above equation, we can find that the thermodynamic device can still function as a quantum heat engine and generate useful work, even without a temperature difference. We note that when the electric power $\langle W_{\text{out}} \rangle > 0$, the thermal machine operates as a heat engine. (i) If the input energy is negative, i.e., $\langle W_I \rangle < 0$, the efficiency of the heat engine is given by

$$\langle \eta \rangle = \frac{\langle W_{\text{out}} \rangle}{(1 - T_l/T_{\text{ph}}) \langle Q_{\text{ph}} \rangle}. \quad (15)$$

Such definition of the efficiency is consistent with the energy efficiency of steady-state thermoelectric transport, e.g., at the Carnot limit $\langle W_{\text{out}} \rangle / \langle Q_{\text{ph}} \rangle = 1 - T_l / T_{\text{ph}}$, the efficiency at Eq. (15) becomes the unit. (ii) When the input energy is nonnegative, i.e. $\langle W_I \rangle \geq 0$, the efficiency of the heat engine becomes [18]

$$\langle \eta \rangle = \frac{\langle W_{\text{out}} \rangle}{(1 - T_l / T_{\text{ph}}) \langle Q_{\text{ph}} \rangle + \langle W_I \rangle}. \quad (16)$$

According to the thermodynamic second law, the thermoelectric engine efficiency is always upper bounded by $\langle \eta \rangle \leq 1$ [16, 72].

In contrast for the elastic heat engine, it is known that $\langle Q_{\text{ph}} \rangle = 0$ in absence of the inelastic electron-phonon scattering. Thus, the average input work is reduced to $\langle W_I \rangle = -(\langle E_l \rangle + \langle E_r \rangle)$. Meanwhile, the entropy production of Equation (14) is simplified to $T_l \langle S \rangle = -\langle W_{\text{out}} \rangle + \langle W_I \rangle$, and the thermodynamic efficiency denotes

$$\langle \eta \rangle = \theta(\langle W_I \rangle) \langle W_{\text{out}} \rangle / \langle W_I \rangle, \quad (17)$$

with $\theta(x) = 1$ for $x > 0$ and $\theta(x) = 0$ for $x \leq 0$. It should note that the input energy of an elastic quantum heat engine originates entirely from the driving energy $W_I = -(\langle E_l \rangle |_{\text{geo}} + \langle E_r \rangle |_{\text{geo}})$, and $\langle E_l \rangle |_{\text{dyn}} + \langle E_r \rangle |_{\text{dyn}} \equiv 0$ due to the second law of thermodynamics [9].

III. RESULTS AND DISCUSSIONS

In this section, we will present results derived from periodically-driven double quantum dot setups. Our investigation will encompass two distinct cases: (i) a comparison of thermodynamic performance between elastic and inelastic heat engines with quantum coherence, and (ii) an exploration of the impact of quantum coherence on the inelastic engine.

A. Elastic vs inelastic periodically-driven heat engines

For the periodically-driven elastic heat engines, a straightforward example of such devices is a two-terminal double quantum dots device, where the energy exchange between quantum dots and the phonon reservoirs is isolated, i.e. $\Gamma_{\text{ph}} = 0$. We depict the average work and efficiency of both elastic (the red solid curve) and inelastic (the black solid curve) heat engines as a function of the potential difference $\Delta\mu$ in Fig.2, utilizing Eq.(13) and Eqs. (15)-(16) to compare their performances. Here

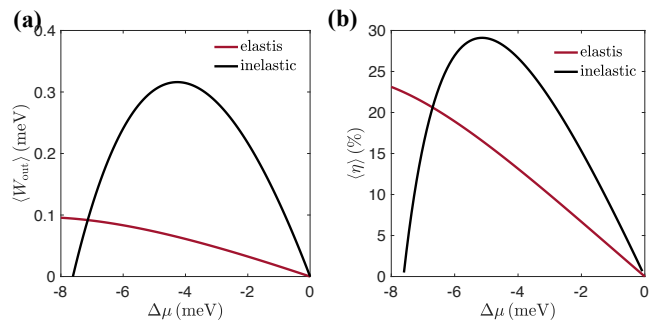


FIG. 2. Comparison of performance between elastic and inelastic quantum heat engines. (a) The average output electric work $\langle W_{\text{out}} \rangle$, (b) average efficiency $\langle \eta \rangle$ as a function of $\Delta\mu$ for two-terminal (elastic) and three-terminal (inelastic) heat engines. The energy level modulations are exemplified as $\varepsilon_l = [-1 + 5 \sin(\Omega t)]$ meV, $\varepsilon_r = [1 + 5 \sin(\Omega t + \pi/2)]$ meV, $\Omega = 2\pi/\mathcal{T}$ and $\mathcal{T} = 10^{-12}$ s. The coupling between quantum dots and phonon reservoir for the inelastic and elastic cases are set as $\Gamma_{\text{ph}} = 4$ meV and $\Gamma_{\text{ph}} = 0$, respectively. The other parameters are given by $\mu = 0$, $\Gamma_l = \Gamma_r = 4$ meV, $\Delta = 8$ meV, $k_B T_l = k_B T_r = 10$ meV, and $k_B T_{\text{ph}} = 12$ meV.

quantum coherence is considered for both heat engines. It is found that even without a temperature difference ($T_l = T_r$), the devices can still work as a quantum heat engine and generate useful work, i.e., $\langle W_{\text{out}} \rangle > 0$.

Fig. 2 clearly shows that in a broad voltage bias range (as indicated by the red and black curves for $-8 \text{ meV} < \Delta\mu < 0$), the inelastic quantum heat engine demonstrates substantially higher output work and efficiency compared to its elastic counterpart. This superior performance is attributed to the benefits of inelastic scattering processes, such as inelastic thermoelectricity, which surpasses conventional elastic transport, as proposed by Mahan and Sofo for conventional thermoelectricity [73]. Consequently, we assert that inelastic heat engines incorporating quantum coherence warrant thorough analysis.

B. Thermodynamic performance of the inelastic heat engine

In Fig. 3, we commence the analysis of the thermodynamic performance of the inelastic engine employing a three-terminal double QDs system. It need note that when we naturally include quantum coherence, we mark the calculated quantities (e.g., the output work) with “coherence”. In contrast if we discard quantum coherence, these quantities are marked with “incoherence”. Initially, we examine the output work and efficiency of the engine, depicted in Fig. 3(a) and 3(b), respectively.

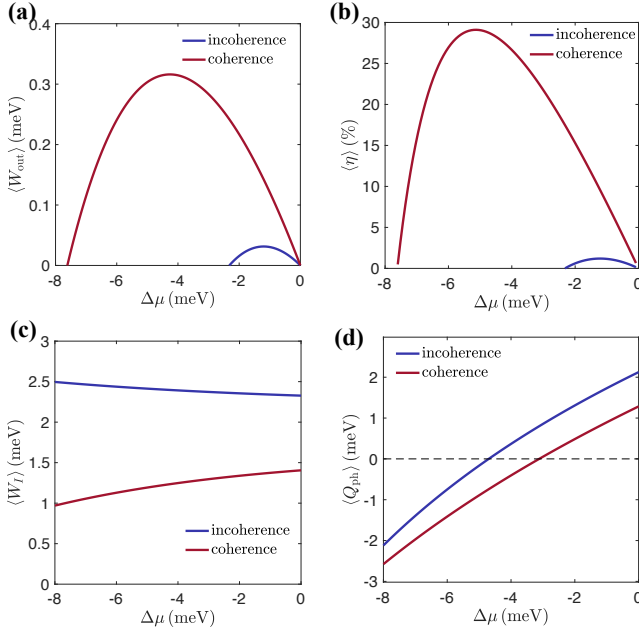


FIG. 3. (a) The average output electric work $\langle W_{\text{out}} \rangle$, (b) average efficiency $\langle \eta \rangle$, (c) the input work done by driving $\langle W_I \rangle$, and (d) average phononic current $\langle Q_{\text{ph}} \rangle$ as a function of $\Delta\mu$ for the coherence and incoherence cases. The energy level modulations are exemplified as $\varepsilon_l = [-1 + 5 \sin(\Omega t)]$ meV, $\varepsilon_r = [1 + 5 \sin(\Omega t + \pi/2)]$ meV, $\Omega = 2\pi/T$ and $T = 10^{-12}$ s. The other parameters are given by $\mu = 0$, $\Gamma_l = \Gamma_r = \Gamma_{\text{ph}} = 4$ meV, $\Delta = 8$ meV, $k_B T_l = k_B T_r = 10$ meV, and $k_B T_{\text{ph}} = 12$ meV.

We observe that the nonzero quantum coherence (off-diagonal elements of system density matrix) yields a significant improvement in the optimal work and efficiency, compared with the counterparts in absence of quantum coherence. More specifically, the maximum output work increases to 0.3 meV as the coherence effect is taken into account, whereas it becomes 0.05 meV by artificially ignoring quantum coherence, see Fig. 3(a). In analogy, the maximum efficiency considering the coherent transport effect lead to a maximum efficiency of 30% (in percentage units), whereas it becomes only 2% during the incoherent transport processes, as shown in Fig. 3(b). (More details of the optimization and comparison can be found in Appendix C.) It's worth noting that the temperatures considered in this analysis are consistent with current experimental conditions [74].

We also scrutinize the impact of quantum coherence on the driving energy W_I and phononic current Q_{ph} . We observe a comparative decrease for the input work W_I due to the quantum coherence in Fig. 3(c). Similarly, the input heat current $\langle Q_{\text{ph}} \rangle$ around $\Delta\mu = 0$ in Fig. 3(d) is reduced to approximately twice the value in absence

of quantum coherence. Hence, quantum coherence enhances the thermodynamic efficiency.

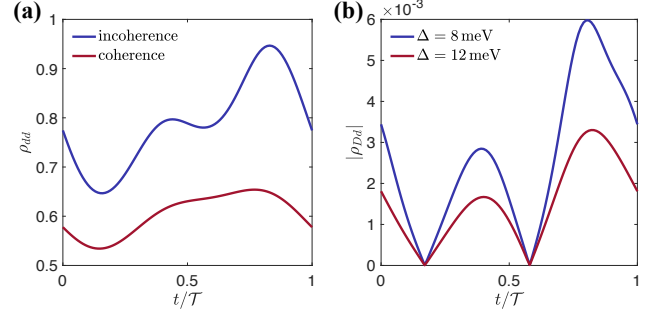


FIG. 4. The density matrix (a) ρ_{dd} with coherence and incoherence as a function of t/T . (b) $|\rho_{Dd}|$ as a function of t/T for different dot-dot tunneling strength Δ . The double QDs energy modulations: $\varepsilon_l = [-1 + 5 \sin(\Omega t)]$ meV, $\varepsilon_r = [1 + 5 \sin(\Omega t + \pi/2)]$ meV, $\Omega = 2\pi/T$ and $T = 10^{-12}$ s. The other parameters are given by $\mu = 0$, $\Gamma_l = \Gamma_r = \Gamma_{\text{ph}} = 4$ meV, $\Delta = 8$ meV, $\Delta\mu = 0$, $k_B T_l = k_B T_r = 10$ meV and $k_B T_{\text{ph}} = 12$ meV.

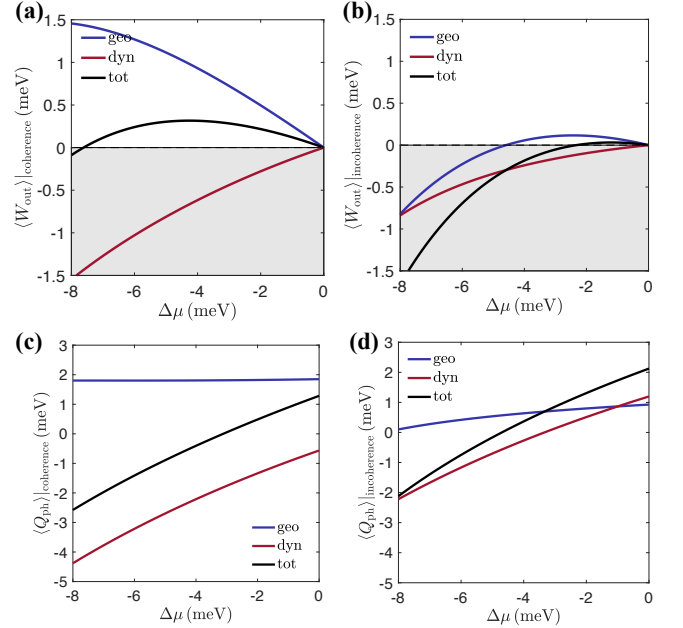


FIG. 5. The average output work $\langle W_{\text{out}} \rangle$ with (a) coherence and (b) incoherence, (c) the photonic current $\langle Q_{\text{ph}} \rangle$ with (c) coherence and (d) incoherence as a function of $\Delta\mu$. The shaded regimes in (a) and (b) denote the useless work. The parameters are the same as in Fig. 3.

Next, we utilize coherence measurement (i.e. $|\rho_{Dd}|$) to quantitatively estimate the quantum coherence during the adiabatic transport [75]. In Fig. 4(a), it is found that

the existence of $|\rho_{Dd}|$ suppresses the diagonal density matrix element ρ_{dd} . And, $|\rho_{Dd}|$ itself in Fig. 4(b) shows finite value and periodic oscillations in one driving period, which is enhanced by the inter-dot tunneling. Thus quantum coherence should not be naively ignored. Considering the contribution of $|\rho_{Dd}|$ to the currents, e.g., the output work $\langle W_{\text{out}} \rangle = (\mu_l - \mu_r) \int_0^T \frac{dt}{\mathcal{T}} \sum_{i=D,d} [-\gamma_{r,i0} \rho_{ii}(t) + \gamma_{r,0i} \rho_{00}(t)] + \frac{1}{4} \sin 2\theta [\tilde{\gamma}_{r,i0} (\rho_{Dd} + \rho_{dD})]$, with the rates $\gamma_{r,i0} = \Gamma_r \lambda_{0i} [1 - f_r(\varepsilon_i)]$, $\gamma_{r,0i} = \Gamma_r \lambda_{0i} f_r(\varepsilon_i)$, $\tilde{\gamma}_{r,i0} = \Gamma_r [1 - f_r(\varepsilon_i)]$, and $\tilde{\gamma}_{r,0i} = \Gamma_r f_r(\varepsilon_i)$ ($\lambda_{0D} = \sin^2 \theta$, $\lambda_{0d} = \cos^2 \theta$) [61, 76], it is known that the output work is dramatically enhanced via the quantum coherence in Fig. 3(a). Therefore, quantum coherence indeed plays a pivotal role in the performance of quantum heat engines.

To provide a further understanding of how coherent and incoherent transport impact output work and phononic currents, we categorize these currents into two distinct components: the geometric and dynamic components [18, 77], as elegantly illustrated in Fig. 5. The former component arises as a consequence of external periodic driving. In contrast, the latter one is attributed to thermodynamic biases, such as differences in chemical potentials and temperature gradients. It's evident that geometric work can counteract the direction of thermodynamic biases, allowing for the realization of a geometric thermoelectric pumping effect, e.g., based on the three-terminal double QDs system [18, 77]. The input work $\langle W_I \rangle$ at Eq. (12) is completely determined by the geometric contribution, expressed as $\langle W_I \rangle = -(\langle E_l \rangle|_{\text{geo}} + \langle E_r \rangle|_{\text{geo}} + \langle Q_{\text{ph}} \rangle|_{\text{geo}})$, based on the first law of thermodynamics, i.e., $\langle E_l \rangle|_{\text{dyn}} + \langle E_r \rangle|_{\text{dyn}} + \langle Q_{\text{ph}} \rangle|_{\text{dyn}} \equiv 0$. The input work is apparently reduced via quantum coherence. Hence, by comparing output work (Figs.5(a)-5(b)), heat current (Figs.5(c)-5(d)), and input work (Fig.3(c)) both at coherence and incoherence cases, it is interesting to note that geometric currents experience dramatic improvement due to quantum coherence effects. Hence, such geometric effect will strongly affect the thermodynamic performance.

Alternatively, in scenarios where pairs of parameters $[\varepsilon_l(t)]$ and $[\varepsilon_r(t)]$ are subjected to periodic driving [78–80], the gauge-invariant Berry curvature is harnessed to describe the system's geometric behavior. This Berry curvature is elegantly expressed as [23, 66, 77]:

$$\mathcal{F}_{\varepsilon_l \varepsilon_r} = \langle \partial_{\varepsilon_l} \varphi | \partial_{\varepsilon_r} \psi \rangle - \langle \partial_{\varepsilon_r} \varphi | \partial_{\varepsilon_l} \psi \rangle, \quad (18)$$

and the geometric contribution of cumulant generating function is described as $\mathcal{G}_{\text{geo}} = -\iint_{\varepsilon_l \varepsilon_r} d\varepsilon_l d\varepsilon_r \mathcal{F}_{\varepsilon_l \varepsilon_r}$ [81]. As shown in Fig. 6, the Berry-phase effect is able to generate geometric particle and heat currents against thermodynamic biases. Specifically, the Berry curvatures

for the particle current, considering both incoherence [Fig. 6(a)] and coherence effects [Fig. 6(b)], promise the existence of geometric currents. However, quantum coherence will further enhance the performance of Berry curvature within the driving zone (rounded by black circles), which finally significantly strengthens geometric contribution to the thermodynamic performance of the inelastic heat engine.

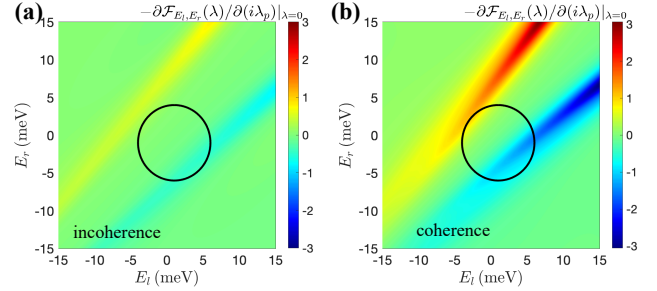


FIG. 6. The contour map in the parameter space of the left QD energy level ε_l and the right QD energy ε_r : Berry curvature for the average particle current $-\partial \mathcal{F}_{\varepsilon_l \varepsilon_r}(\lambda) / \partial (i\lambda_p) |_{\lambda=0}$ (a) with incoherence and (b) coherence cases. The black circle denotes the path of two parameter QDs energy modulations: $\varepsilon_l = [-1 + 5 \sin(\Omega t)] \text{ meV}$, $\varepsilon_r = [1 + 5 \sin(\Omega t + \pi/2)] \text{ meV}$, $\Omega = 2\pi/\mathcal{T}$ and $\mathcal{T} = 10^{-12} \text{ s}$. The other parameters are given by $\mu = 0$, $\Gamma_L = \Gamma_r = \Gamma_{\text{ph}} = 4 \text{ meV}$, $\Delta = 8 \text{ meV}$, $\Delta\mu = 0$, $k_B T_l = k_B T_r = 10 \text{ meV}$ and $k_B T_{\text{ph}} = 12 \text{ meV}$.

IV. CONCLUSION

In summary, we have demonstrated that the quantum coherence can enhance the thermodynamic performance of periodically-driven quantum heat engines. Employing quantum master equations with the full counting statistics method, which conserves quantum coherence, we derived the dynamics and geometric current of coherent quantum heat engine, along with the output work and thermodynamic efficiency. Our results reveal that inelastic quantum heat engine exhibits significantly higher performance compared to their elastic counterpart. The nonzero quantum coherence, characterized as the off-diagonal density matrix elements in eigenbasis, is explicitly exhibited. Various modulations of system parameters, e.g., geometric modulation phase and tunneling strength, on thermodynamic performance are exhibited in Appendix C.

Furthermore, we delved into exploring the impact of quantum coherence on the thermodynamic performance

of the periodically driven inelastic heat engine. Through external modulations with dual parameters and considering the geometric phase, we illustrated that the quantum coherence effect can enhance heat absorption and inelastic currents, consequently improving output work and thermodynamic efficiency. Analyzing the Berry curvature, we further unveiled the mechanism of quantum coherence on geometric currents. It is shown that the curvature is dramatically strengthened via quantum coherence. Therefore, our findings provide physical insights for optimizing periodically-driven inelastic heat engines with quantum coherence resource.

V. ACKNOWLEDGEMENT

This work was supported by the funding for the National Natural Science Foundation of China under Grants No. 12125504, No. 12074281, No. 11935010 and No. 12305050, Jiangsu Key Disciplines of the Fourteenth Five-Year Plan (Grant No. 2021135), the Natural Science Foundation of Jiangsu Higher Education Institutions of China (Grant No. 23KJB140017), and the Opening Project of Shanghai Key Laboratory of Special Artificial Microstructure Materials and Technology.

Appendix A: Full Counting Statistics for Particle and Energy Currents

We briefly introduce the full counting statistics to count the particle and energy flows in the inelastic heat engine. Here, we count the particle and energy flows into the r -th electronic reservoir and the heat current into the ph -th reservoir. Using the two-time measurement protocol [63, 64], one is able to define the characteristic function as

$$\mathcal{Z}(\mathbf{\Lambda}) = \langle e^{i\lambda_p \hat{N}_p(0) + i\lambda_E \hat{H}_E(0) + i\lambda_{ph} \hat{H}_{ph}(0)} e^{-i\lambda_p \hat{N}_p(t) - i\lambda_E \hat{H}_E(t) - i\lambda_{ph} \hat{H}_{ph}(t)} \rangle, \quad (\text{A1})$$

where $\mathbf{\Lambda} = \{\lambda_p, \lambda_E, \lambda_{ph}\}$, $\lambda_{p,E}$ counting parameters for particle and energy flows into the r -th reservoir, and λ_{ph} heat currents into phonon reservoir, respectively. \hat{N}_p represents the number operator for the total particles in the r -th reservoir, \hat{H}_E is the Hamiltonian operator for the r -th reservoir, and \hat{H}_{ph} is the Hamiltonian operator for the phonon reservoir. The time evolution follows the Heisenberg representation, and $\langle \cdot \rangle$ denotes an average with respect to the total initial density operator. This density operator is considered as a factorized form with respect to the central QDs system (S) and the (l , r , and ph) reservoirs. It is expressed as

$$\rho_T(0) = \rho_S(0) \otimes \rho_l(0) \otimes \rho_r(0) \otimes \rho_{ph}(0), \quad (\text{A2})$$

where the equilibrium distribution of ρ_α of the α -th electronic reservoir is given by $\rho_\alpha = \exp[-\beta_\alpha(\hat{H}_\alpha - \mu_\alpha \hat{N}_\alpha)] / Z_\alpha$, with $Z_\alpha = \text{Tr} \left\{ \exp[-\beta_\alpha(\hat{H}_\alpha - \mu_\alpha \hat{N}_\alpha)] \right\}$ representing the partition function, and equilibrium density operator of the phonon reservoir is expressed as $\rho_{ph}(0) = \exp[-\beta_{ph} \hat{H}_{ph}] / Z_{ph}$, with $Z_{ph} = \text{Tr} \left\{ \exp[-\beta_{ph} \hat{H}_{ph}] \right\}$. Actually, Eq. (A1) can be reorganized as

$$\mathcal{Z}_t(\mathbf{\Lambda}) = \text{Tr}[\rho_\Lambda^T(t)], \quad (\text{A3})$$

where the modified density operator is specified as

$$\rho_\Lambda^T(t) = U_{-\Lambda/2}(t) \rho_T(0) U_{\Lambda/2}^\dagger(t). \quad (\text{A4})$$

The propagating operator embedded with counting parameters is given by $U_{-\Lambda/2}(t) = e^{-i\frac{\lambda_{ph}}{2} H_{ph} - i\frac{\lambda_E}{2} H_r - i\frac{\lambda_p}{2} N_r} U(t) e^{i\frac{\lambda_{ph}}{2} H_{ph} + i\frac{\lambda_E}{2} H_r + i\frac{\lambda_p}{2} N_r}$, which can be reexpressed as

$$U_{-\Lambda/2}(t) = e^{-iH_{-\Lambda/2}(t)}, \quad (\text{A5})$$

with the counting-field-dependent total Hamiltonian

$$H_{-\Lambda/2} = e^{-i\frac{\lambda_{ph}}{2} H_{ph} - i\frac{\lambda_E}{2} H_r - i\frac{\lambda_p}{2} N_r} H_T e^{i\frac{\lambda_{ph}}{2} H_{ph} + i\frac{\lambda_E}{2} H_r + i\frac{\lambda_p}{2} N_r}, \quad (\text{A6})$$

and H_T is the total Hamiltonian of the inelastic heat engine. Hence, the t -time cumulant generating function is given by $G_t(\mathbf{\Lambda}) = \partial \ln \mathcal{Z}_t(\mathbf{\Lambda}) / \partial t$. Then the current can be obtained as

$$J_\mu(t) = \left. \frac{\partial G_t(\mathbf{\Lambda})}{\partial(i\lambda_\mu)} \right|_{\mathbf{\Lambda}=0}. \quad (\text{A7})$$

Appendix B: The detailed expression of the evolution $\mathbf{H}(\Lambda)$ for counting the right reservoir

The following is the detailed expression of the evolution $\mathbf{H}(\Lambda)$ for counting the right reservoir:

$$\begin{aligned}
H_{11}(\Lambda) &= -\Gamma_l \cos^2 \theta f_l(E_D) - \Gamma_l \sin^2 \theta f_l(E_d) - \Gamma_r \sin^2 \theta f_r(E_D) - \Gamma_r \cos^2 \theta f_r(E_d), \\
H_{12}(\Lambda) &= \Gamma_l \cos^2 \theta [1 - f_l(E_D)] + \Gamma_r \sin^2 \theta [1 - f_r(E_D)] e^{-i(\lambda_p + \lambda_E E_D)}, \\
H_{13}(\Lambda) &= \Gamma_l \sin^2 \theta [1 - f_l(E_d)] + \Gamma_r \cos^2 \theta [1 - f_r(E_d)] e^{-i(\lambda_p + \lambda_E E_d)}, \\
H_{14}(\Lambda) &= H_{15}(\Lambda) = \frac{1}{2} \Gamma_l \sin \theta \cos \theta [(1 - f_l(E_D)) + (1 - f_l(E_d))] \\
&\quad - \frac{1}{2} \Gamma_r \sin \theta \cos \theta [(1 - f_r(E_D)) e^{-i(\lambda_p + \lambda_E E_D)} + (1 - f_r(E_d)) e^{-i(\lambda_p + \lambda_E E_d)}], \\
H_{21}(\Lambda) &= \Gamma_l \cos^2 \theta f_l(E_D) + \Gamma_r \sin^2 \theta f_r(E_D) e^{i(\lambda_p + \lambda_E E_D)}, \\
H_{22}(\Lambda) &= -\Gamma_l \cos^2 \theta [1 - f_l(E_D)] - \Gamma_r \sin^2 \theta [1 - f_r(E_D)] - \Gamma_{\text{ph}} \cos^2 2\theta [1 + n(\omega_0)], \\
H_{23}(\Lambda) &= \Gamma_{\text{ph}} \cos^2 2\theta e^{i\lambda_{\text{ph}} \omega_0} n(\omega_0), \\
H_{24}(\Lambda) &= H_{25}(\Lambda) = \frac{1}{2} \Gamma_l \sin \theta \cos \theta [1 - f_l(E_d)] - \frac{1}{2} \Gamma_r \sin \theta \cos \theta [1 - f_r(E_d)] + \frac{1}{2} \Gamma_{\text{ph}} \sin 2\theta \cos 2\theta (e^{i\lambda_{\text{ph}} \omega_0} - 1) [1 + n(\omega_0)], \\
H_{31}(\Lambda) &= \Gamma_l \sin^2 \theta f_l(E_d) + \Gamma_r \cos^2 \theta f_r(E_d) e^{i(\lambda_p + \lambda_E E_d)}, \\
H_{32}(\Lambda) &= \Gamma_{\text{ph}} \cos^2 2\theta e^{-i\lambda_{\text{ph}} \omega_0} [1 + n(\omega_0)], \\
H_{33}(\Lambda) &= -\Gamma_l \sin^2 \theta [1 - f_l(E_d)] - \Gamma_r \cos^2 \theta [1 - f_r(E_d)] - \Gamma_{\text{ph}} \cos^2 2\theta n(\omega_0), \\
H_{34}(\Lambda) &= H_{35}(\Lambda) = \frac{1}{2} \Gamma_l \sin \theta \cos \theta [1 - f_l(E_D)] - \frac{1}{2} \Gamma_r \sin \theta \cos \theta [1 - f_r(E_D)] - \frac{1}{2} \Gamma_{\text{ph}} \sin 2\theta \cos 2\theta (e^{-i\lambda_{\text{ph}} \omega_0} - 1) [1 + n(\omega_0)], \\
H_{41}(\Lambda) &= H_{51}(\Lambda) = -\frac{1}{2} \Gamma_l \sin \theta \cos \theta [f_l(E_D) + f_l(E_d)] + \frac{1}{2} \Gamma_r \sin \theta \cos \theta [f_r(E_D) e^{i(\lambda_p + \lambda_E E_D)} + f_r(E_d) e^{i(\lambda_p + \lambda_E E_d)}], \\
H_{42}(\Lambda) &= H_{52}(\Lambda) = \frac{1}{2} \Gamma_l \sin \theta \cos \theta [1 - f_l(E_D)] - \frac{1}{2} \Gamma_r \sin \theta \cos \theta [1 - f_r(E_D)] + \frac{1}{2} \Gamma_{\text{ph}} \sin 2\theta \cos 2\theta (1 + e^{-i\lambda_{\text{ph}} \omega_0}) [1 + n(\omega_0)], \\
H_{43}(\Lambda) &= H_{53}(\Lambda) = \frac{1}{2} \Gamma_l \sin \theta \cos \theta [1 - f_l(E_d)] - \frac{1}{2} \Gamma_r \sin \theta \cos \theta [1 - f_r(E_d)] - \frac{1}{2} \Gamma_{\text{ph}} \sin 2\theta \cos 2\theta (e^{i\lambda_{\text{ph}} \omega_0} + 1) n(\omega_0), \\
H_{44}(\Lambda) &= H_{55}(\Lambda) = -\frac{1}{2} \Gamma_l \sin^2 \theta [1 - f_l(E_D)] - \frac{1}{2} \Gamma_l \cos^2 \theta [1 - f_l(E_d)] - \frac{1}{2} \Gamma_r \cos^2 \theta [1 - f_r(E_D)] - \frac{1}{2} \Gamma_r \sin^2 \theta [1 - f_r(E_d)] \\
&\quad - \frac{1}{2} \Gamma_{\text{ph}} \cos^2 2\theta [1 + 2n(\omega_0)], \\
H_{45}(\Lambda) &= H_{54}(\Lambda) = \frac{1}{2} \Gamma_{\text{ph}} \cos^2 2\theta e^{-i\lambda_{\text{ph}} \omega_0} [1 + n(\omega_0)] + \frac{1}{2} \Gamma_{\text{ph}} \cos^2 2\theta e^{i\lambda_{\text{ph}} \omega_0} n(\omega_0).
\end{aligned} \tag{B1}$$

The counting parameters set denotes $\Lambda = \{\lambda_p, \lambda_E, \lambda_{\text{ph}}\}$, $\Gamma_i = 2\pi \sum_k |\gamma_{i,k}|^2 \delta(E - \varepsilon_{i,k})$ is the dot-electronic reservoir hybridization energy, and $\Gamma_{\text{ph}} = 2\pi \sum_q \lambda_q^2 \delta(\omega - \omega_q)$ is the coupling energy of the phonon bath. $f_i(\varepsilon_i) = \{\exp[(\varepsilon_i - \mu_i)/k_B T_i] + 1\}^{-1}$ is the Fermi-Dirac distribution for the electronic reservoir with chemical potential μ_i and the temperature T_i , and $n(\omega_0) = [\exp(\omega_0/k_B T_{\text{ph}}) - 1]^{-1}$ is the Bose-Einstein distribution function in the phonon reservoir with the temperature T_p and energy gap $\omega_0 = E_D - E_d$.

Appendix C: Performance of the inelastic coherently engines with different modulation phase, coherent tunneling strength

Here, we aim to investigate the impact of various parameters, such as the tunneling strength between the double quantum dots and the modulation phase, on efficiency and output work, without making specific parameter selections.

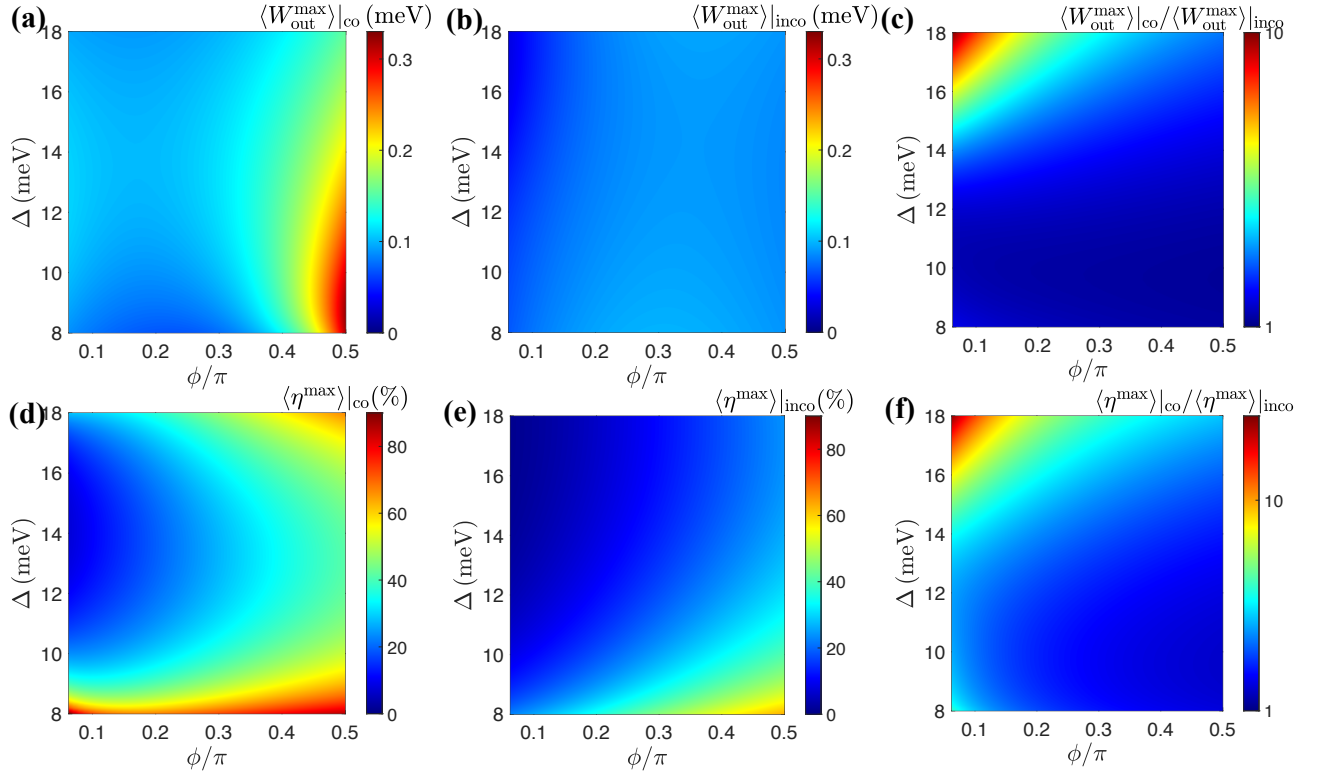


FIG. 7. (a) The coherent maximum output work $\langle W_{\text{out}}^{\text{max}} \rangle_{\text{co}}$, (b) the maximum output work $\langle W_{\text{out}}^{\text{max}} \rangle_{\text{inco}}$, (c) the ratio of the coherent and incoherent maximum work $\langle W_{\text{out}}^{\text{max}} \rangle_{\text{co}} / \langle W_{\text{out}}^{\text{max}} \rangle_{\text{inco}}$, (d) the coherent maximum efficiency $\langle \eta \rangle_{\text{co}}^{\text{max}}$, (e) the incoherent maximum efficiency $\langle \eta \rangle_{\text{inco}}^{\text{max}}$, (f) the ratio of the coherent and incoherent maximum efficiency ratio $\langle \eta \rangle_{\text{co}}^{\text{max}} / \langle \eta \rangle_{\text{inco}}^{\text{max}}$ vs modulation phase ϕ and tunneling strength Δ . The parameters are given by $\mu = 0$, $\Gamma_l = \Gamma_R = \Gamma_{\text{ph}} = 4 \text{ meV}$, $k_B T_l = k_B T_r = 10 \text{ meV}$ and $k_B T_{\text{ph}} = 12 \text{ meV}$. The energy modulations are exemplified as $\varepsilon_l = [-1 + 5 \sin(\Omega t)] \text{ meV}$, $\varepsilon_r = [1 + 5 \sin(\Omega t + \pi/2)] \text{ meV}$, $\Omega = 2\pi/\mathcal{T}$ and $\mathcal{T} = 10^{-12} \text{ s}$, $\mu = 0$.

To begin, we explore how coherent transport behaves with respect to these parameters. In Fig. 7, we present the average output work and efficiency of the heat engine as functions of the tunneling strength (Δ) and the phase (ϕ). For each configuration, we optimize performance by adjusting the chemical potential difference (i.e., the chemical potential difference $\Delta\mu$ at maximum efficiency and work). Fig. 7(a) reveals that coherent transport has a pronounced impact on the maximum output work. For instance, with $\phi = \pi/2$ and $\Delta = 8 \text{ meV}$, the maximum work increases from 0.1 meV to 0.4 meV, due to quantum coherence. We also calculate the enhancement ratio $\langle W_{\text{out}}^{\text{max}} \rangle_{\text{co}} / \langle W_{\text{out}}^{\text{max}} \rangle_{\text{inco}}$ for different tunneling strengths and modulation phases, as shown in Fig. 7(c). This enhancement ratio can be as high as 10, indicating a substantial improvement in work with increasing tunneling strength and decreasing phase.

Moreover, as shown in Fig. 7, although the modulation phase ϕ can increase the magnitude of the geometric current, it doesn't consistently improve the overall performance of heat engines. This discrepancy can be attributed to the potential inconsistency between the direction of geometric and dynamical currents, which can lead to a reduction of the total magnitude of nonequilibrium currents in the system. Meanwhile, the efficiency is optimized when the phase is either small or large, as illustrated in Figs. 7(c) and 7(d). Additionally, the tunneling strength between the quantum dots plays an important role in enhancing quantum coherence. As shown in Figs. 7(a) and 7(b). These results emphasize the crucial role of quantum coherence in inelastic heat engines.

[1] Ronnie Kosloff, "Quantum thermodynamics: A dynamical viewpoint," *Entropy* **15**, 2100 (2013).

[2] Sai Vinjanampathy and Janet Anders, "Quantum thermal

- modynamics,” *Contemporary Physics* **57**, 545 (2016).
- [3] G. Benenti, G. Casati, K. Saito, and R. S. Whitney, “Fundamental aspects of steady-state conversion of heat to work at the nanoscale,” *Phys. Rep.* **694**, 1 (2017).
- [4] L. Arrachea, “Energy dynamics, heat production and heat–work conversion with qubits: toward the development of quantum machines,” *Reports on Progress in Physics* **86**, 036501 (2023).
- [5] U. Seifert, “Stochastic thermodynamics, fluctuation theorems and molecular machines,” *Rep. Prog. Phys.* **75**, 126001 (2012).
- [6] Artur M. Lacerda, Archak Purkayastha, Michael Kewming, Gabriel T. Landi, and John Goold, “Quantum thermodynamics with fast driving and strong coupling via the mesoscopic leads approach,” *Phys. Rev. B* **107**, 195117 (2023).
- [7] H. Haug and A. P. Jauho, *Quantum Kinetics in Transport and Optics of Semiconductors* (Springer-Verlag Berlin Heidelberg, 2008).
- [8] B. Sothmann, R. Sánchez, and A. N. Jordan, “Thermoelectric energy harvesting with quantum dots,” *Nanotechnology* **26**, 032001 (2015).
- [9] J.-H. Jiang and Y. Imry, “Linear and nonlinear mesoscopic thermoelectric transport with coupling with heat baths,” *C. R. Phys.* **17**, 1047 – 1059 (2016).
- [10] L. Buffoni, A. Solfanelli, P. Verrucchi, A. Cuccoli, and M. Campisi, “Quantum measurement cooling,” *Phys. Rev. Lett.* **122**, 070603 (2019).
- [11] Y. Hasegawa, “Quantum thermodynamic uncertainty relation for continuous measurement,” *Phys. Rev. Lett.* **125**, 050601 (2020).
- [12] J. V. Koski, V. F. Maisi, T. Sagawa, and J. P. Pekola, “Experimental observation of the role of mutual information in the nonequilibrium dynamics of a maxwell demon,” *Phys. Rev. Lett.* **113**, 030601 (2014).
- [13] Kaonan Micadei, John P. S. Peterson, Alexandre M. Souza, Roberto S. Sarthour, Ivan S. Oliveira, Gabriel T. Landi, Tiago B. Batalhao, Roberto M. Serra, and E. Lutz, “Reversing the direction of heat flow using quantum correlations,” *Nature Communications* **10**, 2456 (2019).
- [14] T. K. Saha, J. Ehrich, M. Gavrillov, S. Still, D. A. Sivak, and J. Bechhoefer, “Information engine in a nonequilibrium bath,” *Phys. Rev. Lett.* **131**, 057101 (2023).
- [15] B. Bhandari, P. T. Alonso, F. Taddei, F. von Oppen, R. Fazio, and L. Arrachea, “Geometric properties of adiabatic quantum thermal machines,” *Phys. Rev. B* **102**, 155407 (2020).
- [16] J. Liu, K. A. Jung, and D. Segal, “Periodically driven quantum thermal machines from warming up to limit cycle,” *Phys. Rev. Lett.* **127**, 200602 (2021).
- [17] L. M. Cangemi, V. Cataudella, G. Benenti, M. Sassetti, and G. De Filippis, “Violation of thermodynamics uncertainty relations in a periodically driven work-to-work converter from weak to strong dissipation,” *Phys. Rev. B* **102**, 165418 (2020).
- [18] J. Lu, Z. Wang, J. Peng, C. Wang, J.-H. Jiang, and J. Ren, “Geometric thermodynamic uncertainty relation in a periodically driven thermoelectric heat engine,” *Phys. Rev. B* **105**, 115428 (2022).
- [19] P. A. Erdman, A. Rolandi, P. Abiuso, M. Perarnau-Llobet, and F. Noé, “Pareto-optimal cycles for power, efficiency and fluctuations of quantum heat engines using reinforcement learning,” *Phys. Rev. Res.* **5**, L022017 (2023).
- [20] F. Cavaliere, L. Razzoli, M. Carrega, G. Benenti, and M. Sassetti, “Hybrid quantum thermal machines with dynamical couplings,” *Iscience* **26** (2023), 10.1103/RevModPhys.81.1665.
- [21] Y. Xiao, D. Liu, J. He, L. Zhuang, W.-M. Liu, L.-L. Yan, and J. Wang, “Thermodynamics and fluctuations in finite-time quantum heat engines under reservoir squeezing,” *Phys. Rev. Res.* **5**, 043185 (2023).
- [22] Y. Hino and H. Hayakawa, “Geometrical formulation of adiabatic pumping as a heat engine,” *Phys. Rev. Res.* **3**, 013187 (2021).
- [23] A. Bohm, A. Mostafazadeh, H. Koizumi, Q. Niu, and J. Zwanziger, *The Geometric phase in quantum systems* (Springer-Verlag, New York, 2003).
- [24] Z. Wang, L. Q. Wang, J. Z. Chen, C. Wang, and J. Ren, “Geometric heat pump: Controlling thermal transport with time-dependent modulations,” *Frontiers of Physics* **17**, 13201 (2022).
- [25] T. Baumgratz, M. Cramer, and M. B. Plenio, “Quantifying coherence,” *Phys. Rev. Lett.* **113**, 140401 (2014).
- [26] A. Streltsov, G. Adesso, and M. B. Plenio, “Colloquium: Quantum coherence as a resource,” *Rev. Mod. Phys.* **89**, 041003 (2017).
- [27] O. Karlström, H. Linke, G. Karlström, and A. Wacker, “Increasing thermoelectric performance using coherent transport,” *Phys. Rev. B* **84**, 113415 (2011).
- [28] R. Uzdin, A. Levy, and R. Kosloff, “Equivalence of quantum heat machines, and quantum-thermodynamic signatures,” *Phys. Rev. X* **5**, 031044 (2015).
- [29] S.-H. Su, C.-P. Sun, S.-W. Li, and J.-C. Chen, “Photoelectric converters with quantum coherence,” *Phys. Rev. E* **93**, 052103 (2016).
- [30] K. Brandner, M. Bauer, and U. Seifert, “Universal coherence-induced power losses of quantum heat engines in linear response,” *Phys. Rev. Lett.* **119**, 170602 (2017).
- [31] W. Niedenzu, V. Mukherjee, A. Ghosh, A. G. Kofman, and G. Kurizki, “Quantum engine efficiency bound beyond the second law of thermodynamics,” *Nat. Commun.* **9** (2018).
- [32] K. Ptaszyński, “Coherence-enhanced constancy of a quantum thermoelectric generator,” *Phys. Rev. B* **98**, 085425 (2018).
- [33] P. A. Camati, J. F. G. Santos, and R. M. Serra, “Coherence effects in the performance of the quantum otto heat engine,” *Phys. Rev. A* **99**, 062103 (2019).

- [34] G. Francica, F. C. Binder, G. Guarnieri, M. T. Mitchison, J. Goold, and F. Plastina, “Quantum coherence and ergotropy,” *Phys. Rev. Lett.* **125**, 180603 (2020).
- [35] K. Hammam, Y. Hassouni, R. Fazio, and G. Manzano, “Optimizing autonomous thermal machines powered by energetic coherence,” *New J. Phys.* **23**, 043024 (2021).
- [36] J. Liu and D. Segal, “Coherences and the thermodynamic uncertainty relation: Insights from quantum absorption refrigerators,” *Phys. Rev. E* **103**, 032138 (2021).
- [37] Tharon Holdsworth and Ryoichi Kawai, “Heat pump driven entirely by quantum correlation,” *Phys. Rev. A* **106**, 062604 (2022).
- [38] S. Aimet and H. Kwon, “Engineering a heat engine purely driven by quantum coherence,” *Phys. Rev. A* **107**, 012221 (2023).
- [39] K. Hammam, M. Manzano, and G. De Chiara, “Quantum coherence enables hybrid multitask and multisource regimes in autonomous thermal machines,” [arXiv:2308.16080](https://arxiv.org/abs/2308.16080) (2023).
- [40] K. Brandner, M. Bauer, M. T. Schmid, and U. Seifert, “Coherence-enhanced efficiency of feedback-driven quantum engines,” *New Journal of Physics* **17**, 065006 (2015).
- [41] Gabriel T. Landi and Mauro Paternostro, “Irreversible entropy production: From classical to quantum,” *Rev. Mod. Phys.* **93**, 035008 (2021).
- [42] T. Van Vu and K. Saito, “Finite-time quantum landauer principle and quantum coherence,” *Phys. Rev. Lett.* **128**, 010602 (2022).
- [43] J.-H. Jiang, O. Entin-Wohlman, and Y. Imry, “Thermoelectric three-terminal hopping transport through one-dimensional nanosystems,” *Phys. Rev. B* **85**, 075412 (2012).
- [44] J.-H. Jiang, O. Entin-Wohlman, and Y. Imry, “Hopping thermoelectric transport in finite systems: Boundary effects,” *Phys. Rev. B* **87**, 205420 (2013).
- [45] K. Yamamoto, O. Entin-Wohlman, A. Aharony, and N. Hatano, “Efficiency bounds on thermoelectric transport in magnetic fields: The role of inelastic processes,” *Phys. Rev. B* **94**, 121402 (2016).
- [46] R. Wang, C. Wang, J. Lu, and J.-H. Jiang, “Inelastic thermoelectric transport and fluctuations in mesoscopic systems,” *Adv. Phys.: X* **7**, 2082317 (2022).
- [47] L.-L. Nian, B. Zheng, and J.-T. Lü, “Electrically driven photon statistics engineering in quantum-dot circuit quantum electrodynamics,” *Phys. Rev. B* **107**, L241405 (2023).
- [48] J. Lu, R. Wang, C. Wang, and J.-H. Jiang, “Brownian thermal transistors and refrigerators in mesoscopic systems,” *Phys. Rev. B* **102**, 125405 (2020).
- [49] B. Cleuren, B. Rutten, and C. Van den Broeck, “Cooling by heating: Refrigeration powered by photons,” *Phys. Rev. Lett.* **108**, 120603 (2012).
- [50] O. Entin-Wohlman, Y. Imry, and A. Aharony, “Three-terminal thermoelectric transport through a molecular junction,” *Phys. Rev. B* **82**, 115314 (2010).
- [51] F. Mazza, S. Valentini, R. Bosisio, G. Benenti, V. Giovannetti, R. Fazio, and F. Taddei, “Separation of heat and charge currents for boosted thermoelectric conversion,” *Phys. Rev. B* **91**, 245435 (2015).
- [52] J.-H. Jiang, M. Kulkarni, D. Segal, and Y. Imry, “Phonon thermoelectric transistors and rectifiers,” *Phys. Rev. B* **92**, 045309 (2015).
- [53] J. Lu, R. Wang, J. Ren, M. Kulkarni, and J.-H. Jiang, “Quantum-dot circuit-qed thermoelectric diodes and transistors,” *Phys. Rev. B* **99**, 035129 (2019).
- [54] J.-H. Jiang, “Enhancing efficiency and power of quantum-dots resonant tunneling thermoelectrics in three-terminal geometry by cooperative effects,” *J. Appl. Phys.* **116**, 194303 (2014).
- [55] B. K. Agarwalla, J.-H. Jiang, and D. Segal, “Full counting statistics of vibrationally assisted electronic conduction: Transport and fluctuations of thermoelectric efficiency,” *Phys. Rev. B* **92**, 245418 (2015).
- [56] A. Miller and E. Abrahams, “Impurity conduction at low concentrations,” *Phys. Rev.* **120**, 745–755 (1960).
- [57] G. Lindblad, “On the generators of quantum dynamical semigroups,” *Communications in Mathematical Physics* **48**, 119–130 (1976).
- [58] D. Tupkary, A. Dhar, M. Kulkarni, and A. Purkayastha, “Fundamental limitations in lindblad descriptions of systems weakly coupled to baths,” *Phys. Rev. A* **105**, 032208 (2022).
- [59] A.G. Redfield, “The theory of relaxation processes,” *Adv. Magn. Reson.* **1**, 1–32 (1965).
- [60] S. Juergens, F. Haupt, M. Moskalets, and J. Splettstoesser, “Thermoelectric performance of a driven double quantum dot,” *Phys. Rev. B* **87**, 245423 (2013).
- [61] B. Bhandari and A. N. Jordan, “Continuous measurement boosted adiabatic quantum thermal machines,” *Phys. Rev. Res.* **4**, 033103 (2022).
- [62] A. Purkayastha, G. Guarnieri, M. T. Mitchison, R. Filip, and J. Goold, “Tunable phonon-induced steady-state coherence in a double-quantum-dot charge qubit,” *npj Quantum Inf.* **6**, 27 (2020).
- [63] M. Esposito, U. Harbola, and S. Mukamel, “Nonequilibrium fluctuations, fluctuation theorems, and counting statistics in quantum systems,” *Rev. Mod. Phys.* **81**, 1665–1702 (2009).
- [64] M. Campisi, P. Hänggi, and P. Talkner, “Colloquium: Quantum fluctuation relations: Foundations and applications,” *Rev. Mod. Phys.* **83**, 771–791 (2011).
- [65] Heinz-Peter Breuer and Francesco Petruccione, *The theory of open quantum systems* (Oxford University Press, USA, 2002).
- [66] J. Ren, P. Hänggi, and B. Li, “Berry-phase-induced heat pumping and its impact on the fluctuation theorem,” *Phys. Rev. Lett.* **104**, 170601 (2010).
- [67] N. A. Sinitsyn and I. Nemenman, “The berry phase and the pump flux in stochastic chemical kinetics,” *Europhys*

- Lett. **77**, 58001 (2007).
- [68] W. Nie, G. Li, X. Li, A. Chen, Y. Lan, and S.-Y. Zhu, “Berry-phase-like effect of thermo-phonon transport in optomechanics,” *Phys. Rev. A* **102**, 043512 (2020).
- [69] K. Yamamoto and N. Hatano, “Thermodynamics of the mesoscopic thermoelectric heat engine beyond the linear-response regime,” *Phys. Rev. E* **92**, 042165 (2015).
- [70] S.-S. Gu, S. Kohler, Y.-Q. Xu, R. Wu, S.-L. Jiang, S.-K. Ye, T. Lin, B.-C. Wang, H.-O. Li, G. Cao, and G.-P. Guo, “Probing two driven double quantum dots strongly coupled to a cavity,” *Phys. Rev. Lett.* **130**, 233602 (2023).
- [71] J. Lu, Z. Wang, R. Wang, J. Peng, C. Wang, and J.-H. Jiang, “Multitask quantum thermal machines and cooperative effects,” *Phys. Rev. B* **107**, 075428 (2023).
- [72] J.-H. Jiang, “Thermodynamic bounds and general properties of optimal efficiency and power in linear responses,” *Phys. Rev. E* **90**, 042126 (2014).
- [73] G D Mahan and J O Sofo, “The best thermoelectric,” *Proc. Natl. Acad. Sci. USA* **93**, 7436–7439 (1996).
- [74] J. G. Gluschke, S. Fahlvik Svensson, C. Thelander, and H. Linke, “Fully tunable, non-invasive thermal biasing of gated nanostructures suitable for low-temperature studies,” *Nanotechnology* **25**, 385704 (2014).
- [75] T. Baumgratz, M. Cramer, and M. B. Plenio, “Quantifying coherence,” *Phys. Rev. Lett.* **113**, 140401 (2014).
- [76] B. Bhandari, R. Fazio, F. Taddei, and L. Arrachea, “From nonequilibrium green’s functions to quantum master equations for the density matrix and out-of-time-order correlators: Steady-state and adiabatic dynamics,” *Phys. Rev. B* **104**, 035425 (2021).
- [77] J. Ren, “Geometric thermoelectric pump: Energy harvesting beyond seebeck and pyroelectric effects,” *Chin. Phys. Lett.* **40**, 090501 (2023).
- [78] R. Sánchez, C. López-Monís, and G. Platero, “Coherent spin rotations in open driven double quantum dots,” *Phys. Rev. B* **77**, 165312 (2008).
- [79] M. F. Ludovico, L. Arrachea, M. Moskalets, and D. Sánchez, “Probing the energy reactance with adiabatically driven quantum dots,” *Phys. Rev. B* **97**, 041416 (2018).
- [80] J. Monsel, J. Schulenburg, T. Baquet, and J. Splettstoesser, “Geometric energy transport and refrigeration with driven quantum dots,” *Phys. Rev. B* **106**, 035405 (2022).
- [81] M. V. Berry, “Quantal phase factors accompanying adiabatic changes,” *Proc. R. Soc. London A* **392**, 45 (1984).